Soft Matter

# Penetration and preferential binding of charged nanoparticles to mixed lipid monolayers: interplay of lipid packing and charge density

| | |
|---|---|
| Journal: | *Soft Matter* |
| Manuscript ID | SM-ART-10-2020-001945.R1 |
| Article Type: | Paper |
| Date Submitted by the Author: | 07-Dec-2020 |
| Complete List of Authors: | Chaudhury, Anurag; Indian Institute of Science, Physics<br>Debnath, Koushik; Indian Association for the Cultivation of Science, School of Materials Science<br>Bu, Wei; University of Chicago, Center for Advanced Radiation Sources<br>Jana, Nikhil; Indian Association for the Cultivation of Science, School of Materials Science<br>Basu, Jaydeep; Indian Institute of Science, Physics |
| | |

Soft Matter

ARTICLE TYPE

Cite this: DOI: 00.0000/xxxxxxxxxx

# Penetration and preferential binding of charged nanoparticles to mixed lipid monolayers: interplay of lipid packing and charge density†

Anurag Chaudhury,[a] Koushik Debnath,[b] Wei Bu[c], Nikhil R. Jana[b] and Jaydeep Kumar Basu[a‡]

Received Date
Accepted Date

DOI: 00.0000/xxxxxxxxxx

Designing of nanoparticles (NPs) for biomedical applications or mitigating their cytotoxic effects require microscopic understanding of their interactions with cell membranes. Such insight is best obtained by studying model biomembranes which, however, need to replicate actual cell membranes, especially its compositional heterogeneity and charge. In this work we have investigated the role of lipid charge density and packing of phase separated Langmuir monolayers on penetration and phase specificity of charged quantum dot (QD) binding. Using an ordered and anionic charged lipid in combination with uncharged but variable stiffness lipids we demonstrate how subtle interplay of zwitterionic lipid packing and anionic lipid charge density can affect cationic nanoparticle penetration and phase specific binding. Under identical subphase pH, the membrane with higher anionic charge density displays higher NP penetration. We also observe coalescence of charged lipid rafts floating amidst a more fluidic zwitterionic lipid matrix due to phase specificity of QD binding. Our results suggest effective strategies which can be used to design NPs for diverse biomedical applications as well as in devising remedial actions against their harmful cytotoxic effects especially against respiratory diseases.

## 1 Introduction

Various forms of designer and functional nanoparticles (NPs) have been developed as nanoprobes for various biomedical applications including bioimaging probes, drug delivery carriers and theranostics among others[1–10]. In particular, fluorescent NPs like quantum dots (QDs) having high quantum efficiency are very suitable for in vitro and small animal imaging in general and single molecule imaging applications in complex bioenvironments in particular. It is also well known that the cell-nanoparticle interaction is highly sensitive to the NP surface chemistry and surface charge[11–17] and hence the nanoprobe surface must be appropriately designed for the purpose for which it is meant to be used. For example NPs designed for binding to specific receptors on cell surface or on the cell membrane in general will not be suitable for sub-cellular targeting. In this regard it has been further revealed by us earlier[2,18] that NP uptake by cells can follow membrane raft-mediated pathway or by receptor mediated pathway by subtle tuning of surface properties of the NPs. Similarly, NPs can have pH dependent functionality which can alter its effectiveness in interactions with cells or intracellular organelles[10,19–22]. Cancerous cells, in particular, are known to have a dysregulated pH gradient with a lower extracellular pH[23,24]. So it is important to understand the role of electrolytic environment to affect the NP-membrane interaction. To target healthy cells or for bio-imaging purpose, the penetration of these NPs inside the membranes is undesirable whereas for cancerous cells, endocytosis of these NPs may be required for hyperthermia treatment or chemical pyrolysis inside cancer cells[25–30]. The second aspect of NP-cell interactions, especially with respect to their internalisation or permeability, is in terms of NP cytotoxicity. This is especially significant in the context of interaction of NPs with lung surfactant monolayer due to inhalation of such particles and their deposition in the alveolar region of the lung leading to severe respiratory diseases[31–36]. In vitro studies, which seek to explore the efficiency of nanoparticles for various targeted nano-biotechnological applications or their possible adverse effects on different cells, are necessary in developing improved nanoparticle designs or in remedial actions against their bio-hazardous properties[11,37]. However, due to the inherent complexity of various cell membranes large variability in toxicity and permeation efficiency are often observed for NPs in different cell lines.[37–39] Therefore, the derivation of general prin-

[a] *Department of Physics, Indian Institute of Science, Bangalore 560012, India.*
[b] *School of Materials Science, Indian Association for the Cultivation of Science, Kolkata-700032, India.*
[c] *NSF's ChemMatCARS, University of Chicago, Argonne National Lab,Lemont, IL 60439 USA.*
‡ Tel: +91 080 2293 3281; E-mail:basu@iisc.ac.in
† Electronic Supplementary Information (ESI) available: [details of any supplementary information available should be included here]. See DOI: 10.1039/cXsm00000x/

ciples and factors determining NP interactions and permeability of cellular membranes from in vitro studies is non-trivial. In this regard, fundamental studies that could mimic the interaction of NPs with biomembranes in simplified and highly controlled environment are very important in obtaining microscopic insight.

While hydrophobic, hydrophilic as well as charged (both cationic and anionic) NPs have been designed with the goal of enabling specific applications, charged NPs have been generally found to be more effective in cell membrane penetration due to predominantly anionic charge of most cell membranes. In the context of charged NPs interacting with model biomembranes, supported lipid bilayers (SLB) [40–47] and monolayer membranes at the air-water interface [41,48–52] have been extensively used to explore the nature of interactions. Several studies have focused on the effects of NPs on the fluidity of SLBs reporting either their softening or stiffening depending on the various parameters of the NPs such as size and shape or charge [12,13,45,53–55]. Most studies have focused on single component [9,12,15,50,51,56–58] lipid membranes of various degrees of stiffness. However, recent studies including experiments [18,43,59,60] and molecular dynamics (MD) simulations [61] have suggested enhanced and/or phase-specific binding of charged NPs in multicomponent zwitterionic lipid membranes having coexisting liquid ordered ($L_o$) and disordered ($L_d$) phases. Experiments [18,44,59] and MD simulations [61] suggest preferential binding to the $L_d$ phase and also enhanced binding at the phase boundary. In fact our recent studies, using super-resolution stimulated emission depletion (STED) microscopy, depicted the key role played by dynamical membrane nanodomains in determining NP interaction and binding. [18,62]. As mentioned earlier, most cellular membranes including lung surfactant on lung alveolar cells not only contain lipid compositional heterogeneity but also necessarily contain charged (mostly anionic) lipids. Hence, a more realistic understanding of NP-cell interactions in in-vitro studies can be provided with the use of both phase separated and mixed charged-uncharged lipid based biomimetic membranes. However, very little work has been reported [31,63] on charged NP interaction with mixed charged-uncharged lipid membranes.

In this work, we report on in-situ grazing incidence x-ray scattering (GIXS) studies on the nature of cationic NP binding and permeability onto two-component, nanoscale phase separated, Langmuir monolayers consisting of mixtures of anionic and zwitterionic lipids of different stiffness, at the air-water interface. The charged NPs used in this study consists of Cadmium Selenide (CdSe)/Zinc Sulphide (ZnS) core shell quantum dots (QDs). We studied two different lipid monolayer compositions in which the anionic lipid component, (1,2-dipalmitoyl-sn-glycero-3-phospho-(1-rac-glycerol) (sodium salt) (DPPG), which exists in highly ordered state, was fixed, while systematically varying the stiffness of the zwitterionic lipid as well as the lipid charge density. Detailed analysis of X-ray reflectivity (XR) data from the lipid monolayers suggests that cationic Quantum Dot (CQD) penetration is maximum for monolayers with fluidic zwitterionic (DOPC - 1,2-dioleyl-sn-glycero-3-phosphocholine, denoted O1G1) lipids on water (pH = 6) although the NP coverage is lower compared to identical monolayer on PBS (phosphate-buffered-saline) subphase (pH = 7). Despite the higher CQD surface coverage underneath the O1G1 monolayer on PBS subphase compared to that on water, we did not observe higher penetration of identical CQDs due to their reduced surface charge at higher pH. However, interestingly, we observed clear evidence of preferential binding of the CQDs to the ordered and charged phase of the monolayer (consisting mostly of DPPG) as evidenced from the increased headgroup thickness of the DPPG lipids. Completely opposite behaviour is observed for the monolayer with stiffer zwitterionic lipid (DPPC - 1,2-dipalmitoyl-sn-glycero-3-phosphocholine), denoted P2G1, on PBS. There seems to be partial penetration of the CQDs into the monolayer and the preferential phase selectivity is weaker with the lipid headgroup sizes reducing instead of increasing as in O1G1. Grazing incidence X-ray diffraction (GID) studies reveal subtle effects in terms of how the CQDs interact with the monolayers as evidenced from the changes in the ordered nanodomain sizes. For O1G1 on water the raft-like $L_o$ nanodomains, consisting predominantly DPPG lipids, considerably shrink in size due to CQD binding and strong penetration while for O1G1 on PBS we observe nanodomain coarsening which is consistent with increased headgroup size and out-of-plane coherence length. Our results provides microscopic insight into the subtle interplay of lipid packing and charge density, nanoparticle charge which determine the penetration and phase selective binding and interaction of NPs with cell membranes which can help in several aspects in designing NPs for their nano-biotechnological applications in drug delivery, bioimaging as well as in mitigating their cytotoxic effects.

## 2 Experimental details

### 2.1 Materials

1,2-dipalmitoyl-sn-glycero-3-phosphocholine (DPPC),1,2-dioleyl-sn-glycero-3-phosphocholine(DOPC) and 1,2-dipalmitoyl-sn-glycero-3-phospho-(1-rac-glycerol) (sodium salt) (DPPG) phospholipids were purchased from Avanti polar lipids. HPLC grade chloroform was purchased from Sigma-Aldrich and used to prepare the stock solution of the phospholipids. Sodium dihydrogen phosphate ($NaH_2PO4$), disodium hydrogen phosphate ($Na_2HPO_4$), potassium chloride (KCl) and sodium chloride (NaCl) were purchased from Sigma-Aldrich and used to prepare phosphate buffer solution.The buffer was maintained at a pH of 7. Ultrapure deionized water with a resistivity of 18.2 $M\Omega.cm$ was used to prepare the buffer solution as well as the subphase for the monolayer studies. Red emissive cationic core/shell quantum dots (QDs) of average hydrodynamic diameter 22 nm with Cadmium Selenide core and Zinc Sulphide shell were prepared by our previously reported method [64]. The QDs were made hydrophilic via polyacrylate coating by using acrylate monomeric ligands. The synthesis protocol along with their characterization is available in the ESI.†

### 2.2 Methods

Lipid solutions were prepared for DOPC, DPPC and DPPG in spectrograde chloroform. The lipids stocks were mixed to prepare DOPC:DPPG=1:1 or DPPC:DPPG=2:1 solutions. DOPC:DPPG(1:1) or DPPC:DPPG(2:1) were spread onto the aqueous subphase (volume of 320 mL) of a 8.9 cm x 42 cm Langmuir trough (Nima Technology Ltd., Coventry, England) maintained at 20.0±0.5$^0$C. The subphase was either de-ionized (DI) water having pH 6 or a freshly prepared and filtered Phosphate Buffered Saline (PBS) maintained at pH 7. The surface pressure was measured with a precision of 0.1 mN/m using a Wilhelmy balance and a Whatman filter paper Wilhemy plate. After solvent evaporation (15 min), the monolayer was compressed and expanded once with a barrier speed of 7.5 $cm^2/min$ in order to create a homogeneous floating Langmuir film. Between measurements with NPs, the Langmuir-Blodgett (LB) trough was cleaned thrice with ethanol (95%) and twice with DI water and once with chloroform. Addition of 10 nM CQDs was carried out using a micropipette to inject the CQD aliquot from outside the barriers into the subphase with the mixed monolayer in a compressed state having a surface pressure of 26 mN/m and maintained at a subphase temperature of 20$^0$C. The subphase was then gently stirred using an L-shaped stirrer gently without disturbing the compressed monolayer for 10-15 minutes to properly mix the CQDs in the subphase. X-ray measurements were carried out after stabilized dissolution of the CQDs.

### 2.3 Grazing Incidence X-ray Scattering (GIXS)

The GIXS experiments were performed at beamline 15-ID-C ChemMatCARS at the Advanced Photon Source (APS) at Argonne National Laboratory with the following parameters: X-ray beam wavelength, $\lambda$, of 1.239 Å, horizontal and vertical beam size of 2 mm and 20 $\mu$m, respectively, leading to a beam footprint of 2 mm x 1.26 cm. The detector used was the PILATUS 100 K (Dectris) set to single-photon counting mode. Two sets of slits, one placed in front of the detector and the other placed 280 mm from the sample, were used to minimize intense low-angle scattering. For GIXS experiments, the sample environment was enclosed within a box and purged with Helium to avoid water vapour accumulation which will attenuate the scattered signal from the sample, and the Oxygen level was kept below 2% to avoid radiation damage of the lipids. During the measurements, the sample was horizontally translated by 2 mm to a fresh location after regular intervals to avoid prolonged beam exposure.

#### 2.3.1 X-ray reflectivity (XR)

The XR experiments on the pristine monolayers were performed at a lateral surface pressure of 32 mN/m and 26 mN/m at temperature of 20.0±0.5$^0$C and after adding the CQDs while maintaining a constant surface pressure of 26mN/m. XR is measured as a function of the vertical scattering vector component ($q_z$). XR probes the electron density variation $\rho$(z) of the vertical structure of the layers normal to the air/water interface. The coherent scattering length density (SLD), $\rho_s(z)$ distribution, normal to a sample's surface and averaged over the footprint of the beam on the sample, is obtained through the analysis of specular reflectometry data. $\rho_s(z)$ is a value unique to a particular chemical composition and is proportional to the mass density and thereby, the electron density. A slab model was used to represent the monolayer as a stack of slabs, with each slab having a constant thickness and electron density or SLD. The $\rho_s(z)$ profile was laterally averaged over both the ordered and disordered parts of the monolayer under the footprint of the X-ray beam and was calculated by a sum of error functions as:

$$\rho_s(z) = \frac{1}{2}\sum_{n=0}^{N-1} erf(\frac{z-z_i}{\sqrt{2}\sigma})(\rho_{s_{i+1}} - \rho_{s_i}) + \frac{\rho_{s_0}+\rho_{s_N}}{2}, \qquad (1)$$

where erf(z)=$2/\sqrt{\pi}\int_0^z e^{-t^2}dt$, $\sigma$ is the surface roughness from capillary wave theory, N is the number of internal interfaces, $z_i$ is the position of the ith interface, $\rho_{s_i}$ is the SLD of the ith interface, and $\rho_{s_0}$ is the SLD of the aqueous subphase. Modeling of the $\rho_s(z)$ was performed using an open-source reflectivity package, MOTOFIT, which runs in the IGOR Pro environment[65]. Using the recursive Parratt formalism[66], a theoretical reflectometry curve can be calculated and compared to the measured data. Both genetic optimization and Levenberg-Marquardt nonlinear least-squares methods were employed to obtain the best fits with the lowest $\chi^2$ values and structurally meaningful model parameters.

#### 2.3.2 Grazing Incidence Diffraction (GID)

For GID experiments the incidence angle was kept fixed at 0.0906$^0$ while all other parameters were same as for XR measurements. The measured GID data is plotted as contour plots of the intensity as a function of both the horizontal ($\mathbf{q}_{xy}$) and the vertical ($\mathbf{q}_z$) scattering vector components. The lattice spacing $d_{hk}$ was obtained from the in-plane diffraction data as $d_{hk} = 2\pi/\mathbf{q}_{xy}^{hk}$, where the Miller indices h, k were used to index the Bragg peaks needed to calculate the unit cell parameters for the in-plane lattice. The full width at half maximum (fwhm) of the Bragg peaks after correction for the instrumental resolution (0.012 Å$^{-1}$) was used to calculate the in-plane correlation length using the Scherrer formula[67] as follows:

$$L_{xy} \approx 0.9 \times 2\pi/fwhm_{intrinsic}(\mathbf{q}_{xy}) \qquad (2)$$

where,

$$fwhm_{intrinsic}(\mathbf{q}_{xy}) = [fwhm_{measured}(\mathbf{q}_{xy})^2 - fwhm_{resolution}(\mathbf{q}_{xy})^2]^{1/2}. \qquad (3)$$

The fwhm of the Bragg rods was used to estimate the vertical correlation length as: $L \approx 0.9 \times 2\pi/fwhm(\mathbf{q}_z)$[68]. The GID experiments on the pristine monolayers were performed at two lateral surface pressures of 32 mN/m and 26 mN/m and at a temperature of 20.0±0.5$^0$C. After adding the CQDs, GID data was collected while maintaining a constant surface pressure of 26mN/m.

#### 2.3.3 X-ray Fluorescence (XRF)

X-ray fluorescence (XRF) measurements were carried out in GID geometry at incident angles $\mathbf{q}_z < \mathbf{q}_c$ (critical angle of X-ray for air-water interface). A Vortex-60EX multi-cathode energy dispersive X-ray detector (SII Nano Technology USA, Inc.) was placed in a cylindrical well above the interface. It collects fluorescent X-rays from the sample through a Kapton window that caps the bottom of the cylindrical well. Details about the technique can be found in earlier report.[69]

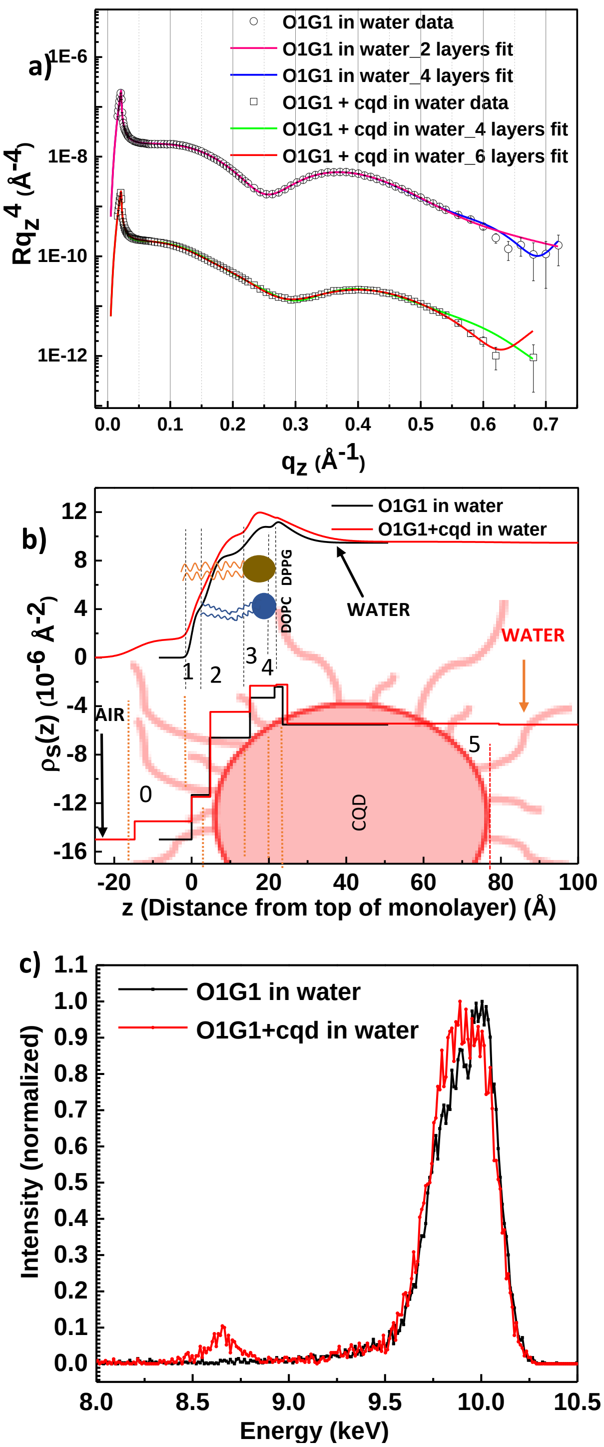


**Fig. 1** a) XR data of pristine DOPC:DPPG(1:1)/O1G1 and after adding CQDs in water subphase. The pink and blue solid lines show fit to the pristine data using 2 and 4 layers respectively, the green solid line shows fit to the O1G1+cqd data with 4 layers assuming there is no CQD layer beneath and the red solid line is the best fit to the O1G1+cqd data with 6 layers assuming the CQD has penetrated the free lipid monolayer (FLM). b) shows the smeared (top) and unsmeared (bottom) scattering length density (SLD) profiles before (corresponding to blue line fit in a)) and after adding 10 nM CQD (corresponding to red line fit in a)). The profile begins with air (left), followed by Tail1, Tail2, Head1 and Head2 layers and then bulk water for the pristine FLM. The layer numbers refer to those mentioned in Table 1. c) shows X-ray Fluorescence (XRF) data taken from pristine O1G1 FLM in pure DI water subphase (black) and O1G1+cqd data (red) in Grazing Incidence Diffraction (GID) geometry.

## 3 Results and discussion

### 3.1 X-ray reflectivity measurements

Figure 1(a) shows normalized XR data and the corresponding fitted profiles for O1G1 FLMs on water before and after incubation with CQDs in the subphase. The extracted ($\rho_s(z)$) profiles, $\rho_s(z)$ of the monolayers corresponding to the best fit in Fig. 1a is presented in Fig. 1b. The main observations that can be gleaned from the $\rho_s(z)$ for the pristine O1G1 monolayer is that merely one head and tail layer does not fit the data well (Fig. 1a, pink solid line), and it is necessary to include two tail and head layers each, which is typical for raft-like lipid monolayers consisting of $L_o$ - $L_d$ phases as observed earlier[70,71]. The DOPC lipid forms the $L_d$ phase and has lower thickness compared to the DPPG lipids which constitute the $L_o$ phase as reported earlier[72,73], leading to a height difference, $\Delta H$ of 3.67 Å. On addition of CQDs, the calculated XR profiles in Fig 1(a) clearly show the need for an additional layer below (in the subphase) and a low density layer above the monolayer (in air) suggestive of not only binding of CQDs but also their deep penetration. Comparative CQD binding models were also used to fit the XR data (ESI Fig. S3)†which were inferior to the best fit profile. Zn fluorescence detected at 8.6 keV in the X-ray fluorescence data, shown in Fig 1(c) clearly confirms the presence of CQDs bound to the monolayer, which was absent in case of XRF signal from the pristine O1G1 monolayer. From the analysed $\rho_s(z)$, it is not easy to discern any phase (raft) selective binding although we observe slight increase in monolayer thickness which could be due to attractions between the cationic CQD and the negatively charged DPPG head group as well as the negatively charged phosphate group in DOPC. To obtain an estimate of the extent of penetration, $t_p$ of the CQD core, one can subtract the CQD layer thickness beneath the monolayer (Table 1) from the core diameter of the CQD. In this case, $t_p$ turns out to be $\sim$ 16 Å. The approximate coverage of the CQDs beneath the FLM was computed using the equation

$$\rho_{s\text{water}}(1-\phi_{\text{QD}}) + \rho_{s\text{QD}} * \phi_{\text{QD}} = \rho^*_{s\text{QD}}, \tag{4}$$

where $\rho_{s\text{water}}$ is the SLD of the bulk water in the subphase, $\phi_{\text{QD}}$ being the area fraction of the CQD layer/coverage area (refer Fig.1 schematic) comprising the core/shell accompanying its ligands and $\rho^*_{s\text{QD}}$ is the effective SLD of the CQD layer obtained from the fit. $\phi_{\text{QD}}$ was found to be around 3%.

In order to explore the effect of both the CQD charge as well as the lipid headgroup interactions, which can be controlled by changing subphase pH, CQDs were also added below the O1G1 monolayer having 1x PBS (buffer with pH 7) subphase. Figure 2 (a) shows normalized XR data and corresponding fit using 4 layers model (Figure 2a, blue line fit) for the pristine FLM. A 2-layer model could not fit the data well (Fig. 2a, pink dashed line) and the fit improved after using a 4-layer model reducing the $\chi^2$ value of the fit to 14.05 from 18.14 for the 4-layer fit. In PBS subphase, $\Delta H$ between the $L_o$-$L_d$ phases was found to be 8.66 Å, which is higher compared to that on water subphase (Table 1). This suggests that the higher pH seems to have affected the headgroup interaction more strongly for the DPPG phase compared to the DOPC phase. For the XR data after addition of CQD, clear evidence of CQD binding was observed, since a 4 layer model did not fit the corresponding XR data very well (Fig 2(a)). Interestingly, even a 6-layer model assuming that the CQD core has penetrated the FLM also could not fit (magenta dotted line) the data well as compared to the model which considered the CQD core was just below the FLM. The competitive models along with their schematics are illustrated the SI. In fact, from Eqn. 4, we find a higher CQD coverage ($\sim$ 7%) beneath the monolayer as

compared to that in water. This is also clearly evident from the higher $\rho_s$ of this layer (Table 1) as well as from the intensity of the Zn peak in XRF data in (ESI Fig. S2a)†. The higher density of adsorbed CQDs for similar sub-phase bulk density beneath the monolayer, probably, arises from the reduced charge on the CQDs as well as increased screening due to presence of counterions allowing their closer packing. What is evident from the $\rho_s(z)$

profiles in Fig 2(b), however, is the clear preferential interaction of CQDs with the DPPG containing charged ordered phase for which the headgroup thickness increases significantly (Table 2) while the disordered phase is not perturbed significantly. This is opposite to the observed behaviour for phase-separated uncharged membranes interacting with charged CQDs.[18,44,59]. The $\rho_s$ of the CQD ligands is larger than the bulk PBS aqueous subphase as found from the XR analysis (Table 1). In the pristine monolayer there are interpenetrating water molecules[74–76] (having lower $\rho_s$ than that of the lipid heads) amongst the heads which lower the effective SLD of the head layers. With the CQD ligands penetrating the PG heads, it is possibly the case that many interpenetrating water molecules are replaced by the higher $\rho_s$ ligands which effectively increase the $\rho_s$ of the head layer. At the same time, we do not observe any significant penetration of CQD core although there is increased disordering of the monolayer as evident from the reduced $\rho_s$ in the tail layers. To incorporate the penetrating ligangs, the tilt angles of the DPPG tails reduced to certain extent (Table 1). The tilt angle from the normal to the interface was calculated by using the equation,

$$\theta_t = \cos^{-1}\frac{l_{tail}}{19.2}, \tag{5}$$

where $l_{tail}$ of DPPG=$l_{tail1}+l_{tail2}$, $l_{tail}$ of DPPC=$l_{tail2}$ is the thickness of the 16-Carbon tail obtained from the XR fit. The thickness of the untilted tail is considered to be 19.2 Å.[76] The reduced penetration could be both due to reduced charge on CQDs as well as screening due to counterions beneath the O1G1 monolayer. The presence of counterions is further confirmed by the appearance of Potasium, Chloride and Phosphate counterionic layer as can be inferred from the 2 keV Phosphorus, 2.6 keV Chlorine and 3.3 keV Potassium peak in the XRF spectrum (inset of ESI Fig. S2a)†, which were not observed in the XRF spectrum for O1G1 in water. This, probably, prevented the CQDs to disrupt the mixed monolayer to the extent they did in water subphase.

In the next system we investigate here, P2G1, we replaced the fluidic part i.e. DOPC with an ordered lipid, DPPC, keeping the charged lipid (DPPG) same as in the earlier measurements and repeated the experiment. From the pressure-area isotherms (ESI Fig. S6a)†, it is evident that this monolayer has a lower area per

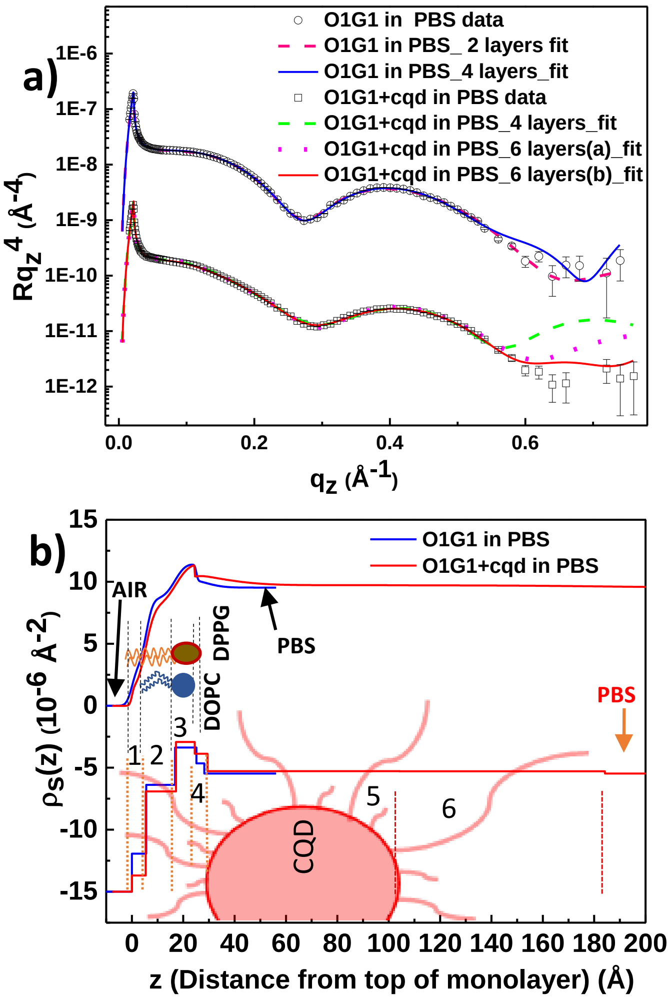


**Fig. 2** a) XR data of pristine DOPC:DPPG(1:1)/O1G1 and after adding CQDs in 1x PBS subphase. The pink dashed line and blue solid line show fit to the pristine data using 2 and 4 layers respectively, the green dashed line shows fit to the O1G1+cqd data with 4 layers assuming there is no CQD layer beneath,the magenta dotted line shows fit with 6 layers assuming the CQD core has penetrated the FLM, and the red solid line is the best fit to the O1G1+cqd data with 6 layers assuming the CQD core is just beneath the FLM with the ligands penetrating the FLM. b) shows the the smeared (top) and unsmeared (bottom) scattering length density (SLD) profiles before (corresponding to blue line fit in a)) and after adding 10 nM CQD (corresponding to red line fit in a)). The profile begins with air (left), followed by Tail1, Tail2, Head1 and Head2 layers and then bulk water for the pristine FLM. The layer numbers refer to those mentioned in Table 1.

lipid compared to O1G1, which is indicative of a higher packing density of the zwitterionic lipid phase as well as possibly an enhanced charged density of the DPPG phase. Figure 3(a) shows the normalized XR data and the corresponding best fit. Similar to O1G1 on PBS the pristine P2G1 XR data collected at 26 mN/m could be well fit using a 4-layer model (Figure 3a, blue line fit) with the corresponding $\rho_s(z)$ shown in Fig 3(b). Once again we observed a small height difference $\Delta H$ of 1 Å between domains with the more ordered and thicker domain corresponding to DPPG. Although the pristine P2G1 FLM was modelled using 2 head layers, At this point it is difficult to conclusively comment on

**Table 1** Parameters obtained from the XR fits of the O1G1 and P2G1 monolayers

| Sample | $l_{Ligand1}$ [#] (Å) | $l_{Tail1}$ (Å) | $l_{Tail2}$ (Å) | $l_{Head1}$ (Å) | $l_{Head2}$ (Å) | $l_{CQD}$ (Å) | $l_{Ligand2}$ (Å) | $\theta_t(^0)^a$ |
|---|---|---|---|---|---|---|---|---|
| **O1G1 in DI water subphase(pH 6)** | | 4.67 (3.67)* | 10.44 (8.39) | 6.35 (11.69) | 2.07 (12.59) | | | 38.1 |
| **After CQD** | 14.72 (1.49) | 4.85 (3.52) | 10.26 (10.52) | 6.82 (12.68) | 2.83 (12.77) | 54.74 (9.55) | | 38.1 |
| **O1G1 in PBS subphase(pH 7)** | | 5.59 (3.07) | 11.22 (8.61) | 8.32 (11.63) | 3.08 (10.35) | | | 28.9 |
| **After CQD** | | 5.34 (1.31) | 11.83 (8.08) | 7.27 (12.07) | 4.97 (11.13) | 74.86 (9.72) | 79.9 (9.71) | 26.6 |
| **P2G1 in PBS subphase (pH 7)** | | 3.71 (2.1) | 12.89 (6.77) | 9.03 (13.14) | 2.69 (11.67) | | | 30.2 [47.8][b] |
| **After CQD** | 16.52 (1.1) | 5.03 (3.65) | 13.4 (9.59) | 8.03 (13.42) | 2.34 (12.28) | 62.63 (9.77) | 68.35 (9.61) | 16.3 [45.7] |

[#] Values in $l_{Ligand1}$, $l_{Tail1}$, $l_{Tail2}$, $l_{Head1}$, $l_{Head2}$, $l_{CQD}$ and $l_{Ligand2}$ columns are the thicknesses of the slabs mentioned in the respective subscripts and these correspond to the slab numbers 0,1,2,3,4.5,6 respectively in the best fit models illustrated in Fig.1,2,3 schematics.
[a] $\theta_t$ is the tilt angle of the lipid tails from the normal to the air-water interface.
[*] Figures in brackets are the Scattering length density values in $10^{-6}$ Å$^{-2}$
[b] Figures in [] are the tilt angles of the DPPC tails while outside [] are the tilt angles of DPPG tails in P2G1 monolayer.

**Table 2** Parameters obtained from X-ray Reflectivity data analyses

| Sample | $\delta t$ (Å) [in %] | $\phi_{QD}$ [in %] | $\delta(H2)$ [in %] |
|---|---|---|---|
| **O1G1 in water subphase** | 1.07 [4.5] | 3 | 37 |
| **O1G1 in PBS subphase (pH 7)** | 1.17 [4.1] | 7 | 61.4 |
| **P2G1 in PBS subphase (pH 7)** | 0.5 [1.8] | 10.1 | -13 |

$\delta t$=Change in monolayer thickness after CQD binding.
$\phi_{QD}$=Coverage area of CQDs beneath the monolayer.
$\delta(H2)$=Relative Change in the Head2(Table 1) thickness after CQD binding.

which lipid head has a larger thickness. From single-component monolayer studies on DPPC and DPPG, the PC and PG head can have a range of thicknesses with different orientations depending upon the surface pressure and temperature.[72–74] The CQDs were added to the mixed membrane P2G1 at 26mN/m and 20$^0$C on PBS subphase maintained at pH 7. A 4-layer model with no CQD layer was allowed to fit the P2G1+cqd data, but the fit was not satisfactory (Figure 3a, green dashed line fit) while a 7-layer model, as illustrated through Figure 3c schematic, could best fit the data. So, there was definite CQD binding, which was also verified by the strong Zn peak from the XRF spectrum (ESI Fig. 2b)†. Interestingly, the 6 layer model which worked for O1G1 on PBS did not give the best fit (Fig. 3a, magenta dotted line). From the fit parameters, only a 0.5 Å increase (Table 2) in the FLM thickness could be seen. On comparing with O1G1+cqd data taken on PBS subphase, the ligands were able to disrupt the DPPG tails because the other lipid component, being a disordered and highly fluidic lipid(ESI Fig. S6)†, there was a large room for the DPPG tails to get disrupted and the DPPG domains to expand into the liquid-ordered DOPC-rich domains (ESI Fig. S7)†. On the contrary, in P2G1, both the lipids are ordered, making the entire mixed monolayer to be a very compact one (ESI Fig. S6)†; hence the tails had no room to become disrupted. In fact, $\theta_t$ of the lipids, especially DPPG, is found to decrease (Table 1) which is a clear indication of the tails getting orientationally ordered. Notably, the $\theta_t$ of DPPG lipids reducing considerably as compared to DPPC also suggests a preferential binding on to charged DPPG phase. However, unlike the O1G1 on PBS case we do seem to observe some penetration of CQDs into the monolayer, $t_p \sim 8$ Å. This penetration is smaller than that observed with O1G1 on water but larger than the same monolayer on PBS. At this stage it is not clear what causes this higher penetration. However, we will discuss this aspect after considering the GID data.

Table 2 suggests that on PBS subphase CQDs have a higher value of $\phi_{QD}$ below the P2G1 monolayer compared to that below O1G1. This might seem contrary to previous study by Roobala et. al.[18],where it was shown that the charged nanoparticles have preferential binding as well as higher penetration into the disordered and more fluidic phase present in a two-component lipid bilayer. However, the ordered component in that case was uncharged. In this case, for P2G1 monolayer the more ordered lipid component is negatively charged and having a higher charge density (suggested from lower area per lipid in ESI Fig. S6a), which possibly leads to higher adsorption and penetration of CQDs compared to O1G1. Table 2 suggests that there was a 13% reduction in Head2 layer. This can only happen if the positively charged QDs repel the exposed positive Choline part of the PC headgroups away from the subphase and compel them to shrink. This implies that the Head2 layer extended into the subpahse probably comprises the DPPC headgroup. So, there are implications to DPPC binding apart from the obvious DPPG binding, PG being

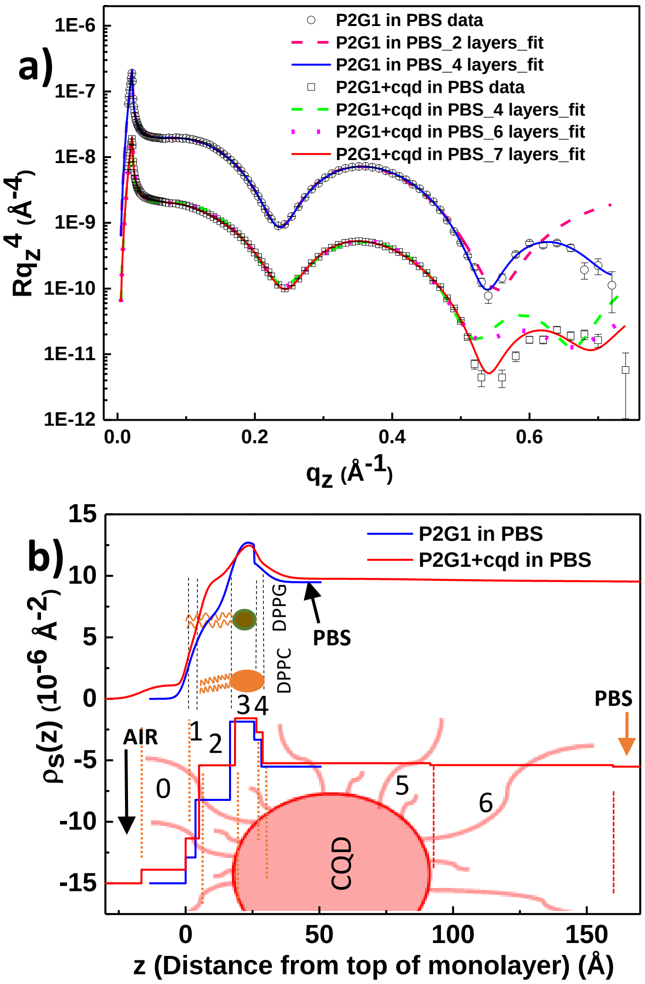


**Fig. 3** a) XR data of pristine DPPC:DPPG(2:1)/P2G1 and after adding CQDs in 0.5x PBS subphase. The pink dashed line and blue solid line show fit to the pristine data using 2 and 4 layers, the green dashed line shows fit to the O1G1+cqd data with 4 layers assuming there is no CQD layer beneath, the magenta dotted line shows fit with 6 layers assuming the CQD core is just below the FLM and the red solid line is the best fit to the O1G1+cqd data with 7 layers assuming the CQD has penetrated the FLM. b) shows the the smeared (top) and unsmeared (bottom) scattering length density (SLD) profiles before (corresponding to blue line fit in a)) and after adding 10 nM CQD (corresponding to red line fit in a)). The pristine P2G1 profile begins with air (left), followed by Tail1, Tail2, Head1 and Head2 layers and then bulk water for the pristine FLM. The layer numbers refer to those mentioned in Table 1.

negatively charged. Such behaviour of the zwitterionic PC headgroup in the proximity of charged species is well-known as already reported [13,17] However, the scenario of preferential binding and other minute structural aspects of the consequences of CQD penetration shall be discussed in the GID section.

### 3.2 Grazing Incidence Diffraction (GID) measurements

Apart from the XR measurements, GID was performed on the same set of monolayers to collect information about the effect of the CQDs on the lattice structural changes of the ordered lipid components in the FLMs. It has been shown earlier that pure DPPG monolayer has a single peak on water at at higher pressures around 32mN/m indicating a hexagonal lattice which gets distorted to produce 2 non-degenerate diffracted peaks on PBS subphase or at lower surface pressures [72,73,77,78]. Our data on O1G1 FLMs at 32 mN/m also showed similar behaviour (ESI Fig. S8,9)†.

Figure 4a shows GID data for the O1G1 monolayer on DI water subphase at 26 mN/m which primarily originates from the ordered and negatively-charged DPPG containing $L_o$ domains. Two peaks were observed, consistent with earlier observations on pristine DPPG monolayers at lower pressure [73,78]. The lower $Q_{xy}$ peak is centred at $Q_Z > 0$ (ESI Fig. S11)†which suggests a transformation from undistorted hexagonal lattice at 32 mN/m to a centred rectangular lattice at 26 mN/m with the lattice parameters as shown in Table 3. Earlier studies have used GID measurements on mixed FLMs containing raft-like domains to estimate these nanodomain sizes [71], $d_n$. On account of having asymmetric coherence lengths, $L_{xy}$, estimated from the respective GID peaks, in Fig. 4a, along [0 2] and [1 1] lattice vectors (Table 3), the DPPG-rich scattering entity is considered to be an ellipsoidal raft/nanodomain. These nanodomains are believed to be floating in the background of a fluidic $L_d$ phase consisting mostly of DOPC lipids. The estimated $d_n$ are also indicated in the Table 3. Figure 4b shows the GID data collected from O1G1 (on DI water subphase) after addition of CQDs. The data shows considerable modification in both the [0 2] and [1 1] peaks. The lattice expands significantly leading to increase in area per molecule, $A_h$ as indicated in Table 3. But most interestingly, we observe a strong reduction of the $d_n$ from $161.7 nm^2$ to $36 nm^2$ suggesting disruption of rafts. On DI water subphase, the CQDs are seen to affect the DPPG tails by increasing the their tilt (azimuthal angles) ($\theta_{NN}$) significantly from $12^0$ to $25.1^0$ towards the nearest neighbour (NN) DPPG molecule of its lattice (Fig. 4c). While GID data indicates strong interaction with the $L_o$ phase containing DPPG, the preferential binding cannot be inferred since the DOPC containing $L_d$ phase does not give rise to any peaks in GID. From Table 3, the out-of-plane coherence length, $\mathbf{L_z}$, estimated from the width of the [1 1] Bragg rod (ESI Fig. S11)†, increased from 15.4 Å to 36.4 Å. It is possible that this enhanced $\mathbf{L_z}$ could emerge due to the CQD ligands (which are longer) which are interspersed with the lipid tails. It can be noted that analysis of the corresponding XR data suggested the possible presence of a ligand layer, fully penetrating the FLM, consistent with the above observation from GID.

For O1G1 FLM on PBS, the peaks were found to have a low intensity in contrast to DI water subphase because of the high background created by the X-ray scattered from the counterionic layer beneath the FLM (ESI Fig. S12)†. For the pristine O1G1 FLM on PBS, $A_h$ is larger while the respective $L_{xy}$ values are much smaller (Table 3), compared to O1G1 FLM on water, suggesting a looser packing of lipids. Also, $d_n$ is considerably smaller compared to O1G1 FLM on DI water. On addition of CQD, the observed increase in $A_h$ is much smaller indicating weaker interaction and reduced penetration, consistent with the information obtained from the corresponding XR data analayis (Table 1). Intriguingly, we do observe a visible increase in the $L_{xy}$ value of the [0 2] peak, leading to an increase in $d_n$ suggesting coalescence of these do-

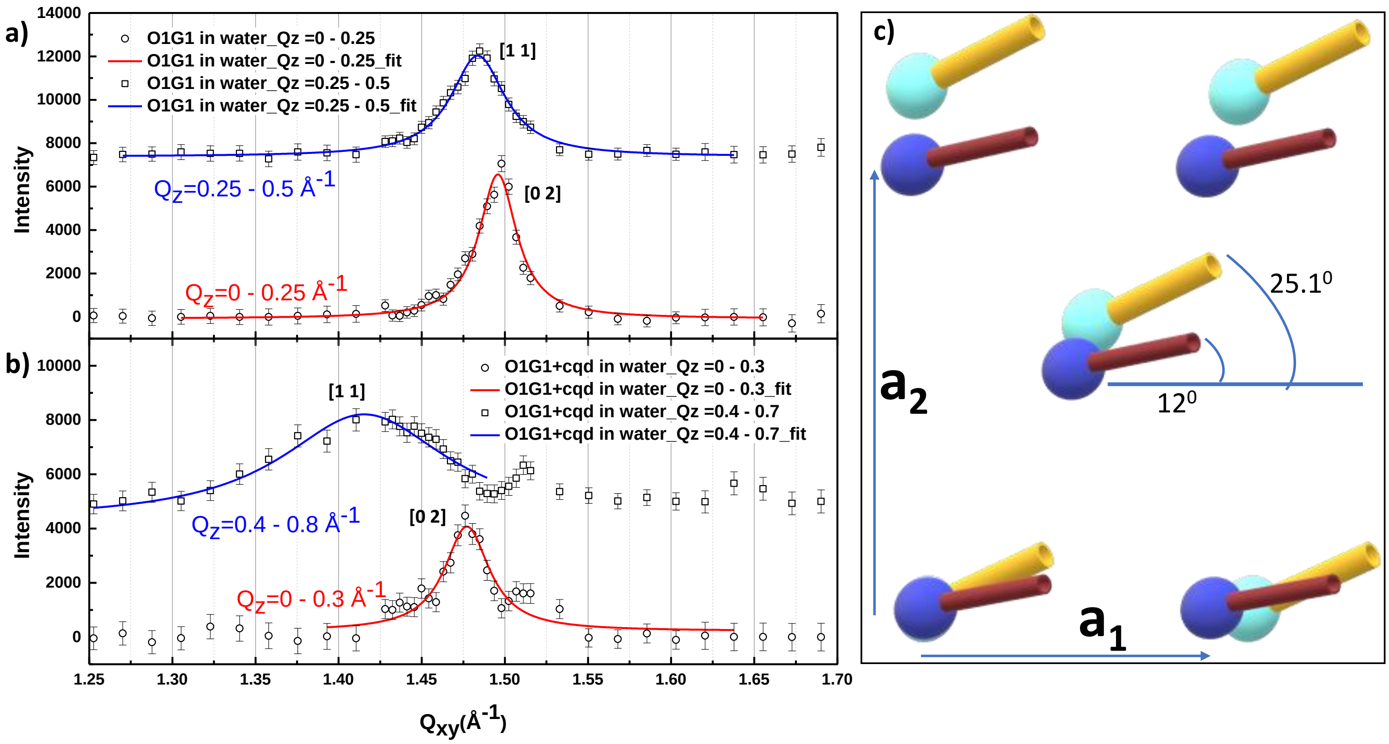


**Fig. 4** GID data of a) pristine DOPC:DPPG(1:1) monolayer and b) after adding 10nM CQDs, collected at 26 mN/m and 20$^0$C in DI water subphase, showing significant lattice distortion in the ordered DPPG lattice. The [1 1] and [0 2] Bragg reflection intensities have been integrated through specific $Q_z$ ranges as depicted in the graphs, and have been shifted vertically for clarity. c) Schematic showing the top view of the DPPG centred-rectangular lattice present in pristine O1G1 FLM in DI water (pH 6) subphase (dark blue balls and brown rods) and the expanded lattice after CQD binding (light blue balls with yellow rods) showing azimuthal tilt towards nearest neighbour.

mains due to CQD binding. Such coalescence must be mediated by the charge of the CQDs which implies the preference of these nanoparticles to bind to the anionic $L_o$ phase. This observation is consistent with the increased head group thickness of the DPPG molecules present in $L_o$ phase as observed from XR.

Figure 5a shows GID data for pristine P2G1 monolayer at 26mN/m and 20$^0$C. The scattering intensity was much higher compared to that from O1G1 monolayers and produced very strong [1 1] and [0 2] peaks. This could be understood from the fact that in P2G1, the entire monolayer area onto which the X-ray footprint is incident, is highly ordered. Opposed to this, in O1G1 monolayer, only a fraction of the monolayer-the DPPG nanodomains-were incoherently contributing to the cumulative intensity leading to the DPPG Bragg peaks. Large coherence lengths (Table 3) were observed along the [0 2] lattice vectors of the centred rectangular DPPG lattice. In fact, in this case the [0 2] peak was an amalgamated diffracted intensity arising from both the liquid-ordered DPPC grains and the DPPG grains. On the other hand, the coherence length along the [1 1] lattice vector is a consequence of the DPPC lattice only, because DPPC is well known from literature to have 2 peaks.[75,77]. This [1 1] peak is broader (implying a lower coherence length) than or comparable to that in O1G1 (on water) as in that case, the [1 1] peak arose from diffraction from the more ordered DPPG lattices. The information about the $\theta_{NN}$ in DPPC and DPPG tails was extracted out from the Bragg peaks and the Bragg rods (ESI Fig. S13)†, the values of which are mentioned in Table 3. From the GID fit parameters, it is clear that after CQD binding to the P2G1 monolayer, there is negligible change in the lattice vectors $\mathbf{a_1}$ and $\mathbf{a_2}$. However the intensities of the [1 1] and [0 2] peaks was found to decrease to a fraction 0.9 and 0.71 respectively after CQD addition. This suggests that the DPPG lattice had been more affected by the preferrential binding of CQDs.

### 3.3 Discussion

There are two main aspects of our study of interaction of CQDs with phase-separated, charged lipid monolayers which emerges from the discussions above: varying penetration in these mixed FLMs and the phenomenon of preferential binding. Our study

brings out the role of lipid packing and charge density of the mixed FLMs which drive these biophysical phenomena at the nanoscale. The primary motive behind this investigation was to observe whether it is the entropy of the zwitterionic lipid component or the charge density of the membrane which determines the extent of binding and penetration of charged nanoparticles. In previous studies, it had been reported that charged nanoparticles prefer to bind to the more fluidic lipid phase in a two component zwitterionic membrane. In this study we have observed that in case of O1G1 FLMs, the CQDs bind to the membrane and from the GID data analysis it is seen that the bound CQDs distort the ordered DPPG lattice and cause the $\theta_{NN}$ of the DPPG acyl chains to

**Table 3** Parameters obtained from GID data analyses

| Sample | a (Å) | b (Å) | $L_{\mathbf{xy}}[11]^*$ (Å) | $L_{\mathbf{xy}}[02]^*$ (Å) | $A_h(\text{Å}^2)^{**}$ | $\theta_{NN}(^0)^{\$}$ | $L^*_{\mathbf{z}}$ (Å) | $\mathbf{d}_n{}^{\#}$ ($nm^2$) |
|---|---|---|---|---|---|---|---|---|
| **O1G1 in DI water(pH 6)** | 4.9 | 8.4 | $148.8 \pm 6.6$ | $225.8 \pm 15.9$ | 41.2 | $12.0 \pm 0.4$ | $15.4 \pm 1.6$ [ $9.5 \pm 0.7$ ][a] | 161.7 |
| **After CQD** | 5.2 | 8.5 | $46.5 \pm 6.2$ | $184.8 \pm 27.8$ | $44.3 \pm 0.2$ | $25.1 \pm 0.4$ | $36.4 \pm 5.1$ [ $11 \pm 1$ ] | 36 |
| **O1G1 in PBS(pH 7)** | $5.15 \pm 0.01$ | 8.46 | $63.4 \pm 9.0$ | $210.3 \pm 30.0$ | $43.6 \pm 0.1$ | $20.8 \pm 0.4$ | $15.1 \pm 4.0$ [ $8.8 \pm 1.0$ ] | 56.3 |
| **After CQD** | 5.28 | 8.48 | $70.4 \pm 7.4$ | $325.8 \pm 79.9$ | $44.8 \pm 0.1$ | $28.9 \pm 0.5$ | $13.8 \pm 4.1$ [ $13.4 \pm 1.3$ ] | 96.9 |
| **P2G1 in PBS(pH 7)** | 4.95 (5.54)[b] | 8.57 (8.57) | $70.8 \pm 2.7$ | $302.4 \pm 10.4$ | 42.4 (47.5) | 0 ($32.3 \pm 0.2$) | $18.6 \pm 0.8$ [ $15.3 \pm 0.8$ ] | 718.2 (93.2) |
| **After CQD** | 4.95 (5.54) | 8.57 (8.57) | $71.0 \pm 2.6$ | $285.5 \pm 13.4$ | 42.4 (47.5) | 0 ($32.8 \pm 0.2$) | $18.5 \pm 0.7$ [ $15.7 \pm 0.9$ ] | 640.2 (88.4) |

*$L_{\text{xy}}[11], L_{\text{xy}}[02], L_{\text{z}}$ are the in-plane coherence lengths along the [1 1] and [0 2] lattice vectors and out-of-plane coherence lengths for the Bragg rods respectively

**$A_h$ is the DPPG head-group area in O1G1, and individual head-group area of DPPC and DPPG in P2G1 nanodomains.

$ Azimuthal angles of the tail tilt towards Nearest Neighbour (NN) in the centred-rectangular lattice.

# $d_n$ = Nanodomain sizes

[a]Values in [] denote the out-of-plane coherence lengths for the [0 2] Bragg rod while without [] correspond to the [1 1] Bragg rods.

[b]The figures in brackets denote the parameters of the DPPC lattice in P2G1, and the figures outside brackets denote the parameters of the DPPG lattice.

The lattice parameters without the standard deviation errors are precise to the least significant digit.

increase although no information can be obtained regarding their binding propentity to the more fludic DOPC phase. This observation confirms that the cationic CQDs bind to the anionic DPPG domains through strong electrostatic interaction. From the XR data analysis , it was observed that the CQDs bound to negatively charged DPPG head-groups and increased the thickness of the DPPG head layer but did not affect the DOPC layer thickness suggesting possibility of preferential binding to the ordered but oppositely charged domains containing, predominantly, DPPG lipids. The salts present in the PBS buffer subphase for the O1G1 FLM plays an important role because the counterionic layer formed beneath the monolayer was found to prevent the charged nanoparticles to infiltrate the monolayer leading to lower penetration and binding. In case of water subphase, the nanoparticles have been found to penetrate the O1G1 monolayer to a greater extent. The subphase environment was also different in terms of pH and also impacted the charge density of the lipids as well as the charge on the CQD surface. The DI water, having a lower pH (=6), increases the surface charge of the CQDs; and the monolayer, being fractionally negatively charged due its DPPG component, caused the higher charged CQDs to attack the mixed lipid membrane to a greater degree. The presence of counter-ions in PBS subphase screened the charge of the CQDs, allowing them to come closer and cover a larger fraction of the area beneath the O1G1 membrane when present in PBS subphase as compared to DI water. The changes are more dramatic in DI water subphase(pH 6) as compared to PBS subphase(pH 7) because of larger surface charge of CQDs at lower pH and also because the DPPG nanodomains, with a lower headgroup area, have a higher surface charge density of 2.427 $e^-/nm^2$ in DI water subphase compared to 2.294 $e^-/nm^2$ in PBS subphase. Although the isotherms of the O1G1 FLMs suggest that the average area per lipid is lower on PBS subphase compared to that on DI water (ESI Fig. S6a)†, the GID data suggests that the mean molecular area of the DPPG lipids alone is lower on DI water subphase. This is expected because at lower pH, the positive counter-ions screen the negative charges of the lipid headgroup, allowing them to pack closely, thus increasing the charge density.[79] This also possibly explains the highest penetration by the CQDs into O1G1 on DI water subphase as observed from the XR analyses. Replacing the fluidic zwitterionic component with an ordered lipid DPPC for the P2G1 system lead to increased overall lipid packing and charge density. As a result we did not observe any significant change in the lattice parameters from GID data analysis after addition of the CQDs. It has been studied that the CQDs reduce the line tension between the domains.[80] In this case too, the CQD core penetrate by around 10-12 Å and in the process, reduce the tension at the boundaries between the lipid nanodomains and reducing their sizes (Table 3). The CQDs possibly squeeze into the lipids and instead of causing disruption, induce more ordering in the tail region. This conform with the XR results, where the tail electron densities were seen to increase - a clear indication of minimal disruption and more ordering in the plane normal to the air-water interface. This is due to the highly compact P2G1 monolayer (ESI Fig. S6b)†which resist the CQDs to cause disordering along the plane normal to the interface. This is the reason why the CQD binding is unable to produce lattice changes in the ordered nanodomains but merely reduce the $d_n$. The mean molecular area of DPPG in P2G1 is less than that in O1G1 (in PBS). GID analysis also suggests that DPPG nanodomains in P2G1 have a sur-

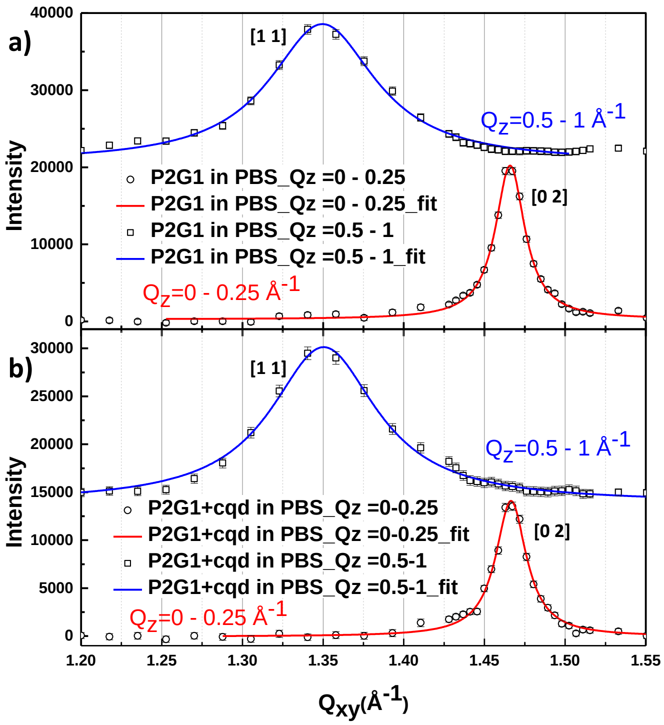


**Fig. 5** GID data of a) pristine DPPC:DPPG(2:1) and b) after adding 10nM CQDs, collected at 26 mN/m and 20$^0$C in PBS subphase, showing minimal lattice distortion in the ordered DPPC and DPPG lattice. The [1 1] and [0 2] Bragg reflection intensities have been integrated through specific $Q_z$ ranges as depicted in the graphs, and have been shifted vertically for clarity.

face charge density of 2.358$e^-/nm^2$ which is higher than those in O1G1 FLM (on PBS subphase). This suggests why penetration of the CQDs was found to be more in case of P2G1 on PBS as compared to O1G1 on same subphase. Further, the intensity of the Bragg peak arising from the DPPG lattices reduces by a larger fraction compared to the other peak arising from DPPC domains after CQD binding. Moreover, $\theta_t$ of DPPG tails was observed to reduce considerably, while DPPC tilt angles did not alter much. This indicates that in such an ordered membrane too, the CQDs prefer DPPG domains to bind to. On the same PBS subphase (pH 7), a striking difference between O1G1 and P2G1 was that the CQDs caused the DPPG rafts to coalesce in O1G1 FLM whereas in P2G1, the CQDs reduced both the DPPC and DPPG raft sizes. In O1G1 the phenomenon of raft coalescence is predominant and seems to lead to enlargement of the negatively charged rafts. It is also noteworthy that $d_n$ of the anionic DPPG nanodomains in P2G1 are 12.75 times larger than the nanodomains present in O1G1. Although the mole fraction of the anionic DPPG molecules in P2G1 is less (as compared to O1G1), such strikingly larger anionic $d_n$ in P2G1 with a higher charge density have probably lead to a larger coverage of the CQDs beneath the P2G1 monolayer as observed from the XR analyses.

## 4 Conclusions

In conclusion, using a combination of XR, GID and XRF techniques we provide microscopic insight into nature of charged nanoparticle interaction with mixed zwitterionic and negatively charged lipid membranes, especially their ability to penetrate and bind in phase specific manner. Contrary to earlier reports, we observe higher preference of QD binding to the more ordered but negatively charge phase. Further, the density of the adsorbed CQDs layer as well as their ability to penetrate the lipid monolayer biomembranes could be tuned by changing ambient pH and, stiffness and structural ordering of the zwitterionic lipid component. Our study also reveals presence of membrane nanodomains and indicates how they are perturbed by CQD interaction due to subtle interplay of entropic and electrostatic effects. We believe this will help the future research in designing specific nanoparticles to target cell membranes with different electrolytic environment and mechano-electrostatic properties for bio-imaging and targeted drug delivery as well as in providing directions to mitigate nanoparticle induced respiratory diseases due to their cytotoxic effects. In general, the results presented here could also be relevant in understanding interactions of other pathogens like viruses or charged biomolecules, which are typically of tens of naonmetres dimensions, with cells.

## Conflicts of interest

There are no conflicts to declare.

## Acknowledgements

The authors thank the Department of Science and Technology, India (SR/NM/Z-07/2015) for the financial support and Jawaharlal Nehru Centre for Advanced Scientific Research (JNCASR) for managing the project. ChemMatCARS Sector 15 is supported by the National Science Foundation under grant number NSF/CHE-1834750. This research used resources of the Advanced Photon Source, a U.S. Department of Energy (DOE) Office of Science User Facility operated for the DOE Office of Science by Argonne National Laboratory under Contract No. DE-AC02-06CH11357. The authors are also thankful to Mr. Ravindra Kumar Yadav, IISc, for his help in the beamline experiments.

## Author contributions

J.K.B. and N.R.J. conceptualized the study. The beamline experiments were performed by A.C. under the supervision of J.K.B. and with assistance from W.B. The synthesis and characterization of the CQDs were performed by K.D. The analysis of the X-ray reflectivity, Grazing Incidence Diffraction and X-ray Fluorescence was performed by A.C. through inputs from J.K.B. and W.B. The first draft was written by A.C. and modified by J.K.B. with inputs from all the authors.

## Notes and references

1 N. R. Jana, *Physical Chemistry Chemical Physics*, 2011, **13**, 385–396.

2 A. Chakraborty and N. R. Jana, *The journal of physical chemistry letters*, 2015, **6**, 3688–3697.

3 S. J. Tan, N. R. Jana, S. Gao, P. K. Patra and J. Y. Ying, *Chemistry of Materials*, 2010, **22**, 2239–2247.

4 C. Dalal and N. R. Jana, *The Journal of Physical Chemistry B*, 2017, **121**, 2942–2951.

5 D. Chenthamara, S. Subramaniam, S. G. Ramakrishnan, S. Krishnaswamy, M. M. Essa, F.-H. Lin and M. W. Qoronfleh, *Biomaterials Research*, 2019, **23**, 1–29.

6 Z. Xue, Q. Sun, L. Zhang, Z. Kang, L. Liang, Q. Wang and J.-W. Shen, *Nanoscale*, 2019, **11**, 4503–4514.

7 S. Parimi, T. J. Barnes and C. A. Prestidge, *Langmuir*, 2008, **24**, 13532–13539.

8 A. Mecke, S. Uppuluri, T. M. Sassanella, D.-K. Lee, A. Ramamoorthy, J. R. Baker Jr, B. G. Orr and M. M. B. Holl, *Chemistry and physics of lipids*, 2004, **132**, 3–14.

9 R. Bhattacharya, S. Kanchi, C. Roobala, A. Lakshminarayanan, O. H. Seeck, P. K. Maiti, K. Ayappa, N. Jayaraman and J. K. Basu, *Soft Matter*, 2014, **10**, 7577–7587.

10 E.-K. Lim, B. H. Chung and S. J. Chung, *Current drug targets*, 2018, **19**, 300–317.

11 A. E. Nel, L. Mädler, D. Velegol, T. Xia, E. M. Hoek, P. Somasundaran, F. Klaessig, V. Castranova and M. Thompson, *Nature materials*, 2009, **8**, 543–557.

12 M. Schulz, A. Olubummo and W. H. Binder, *Soft Matter*, 2012, **8**, 4849–4864.

13 B. Wang, L. Zhang, S. C. Bae and S. Granick, *Proceedings of the National Academy of Sciences*, 2008, **105**, 18171–18175.

14 M. Laurencin, T. Georgelin, B. Malezieux, J.-M. Siaugue and C. Ménager, *Langmuir*, 2010, **26**, 16025–16030.

15 N. Biswas, R. Bhattacharya, A. Saha, N. R. Jana and J. K. Basu, *Physical Chemistry Chemical Physics*, 2015, **17**, 24238–24247.

16 A. Olubummo, M. Schulz, B.-D. Lechner, P. Scholtysek, K. Bacia, A. Blume, J. Kressler and W. H. Binder, *ACS nano*, 2012, **6**, 8713–8727.

17 A. Velikonja, P. B. Santhosh, E. Gongadze, M. Kulkarni, K. Eleršič, Š. Perutkova, V. Kralj-Iglič, N. P. Ulrih and A. Iglič, *International journal of molecular sciences*, 2013, **14**, 15312–15329.

18 R. Chelladurai, K. Debnath, N. R. Jana and J. K. Basu, *Langmuir*, 2018, **34**, 1691–1699.

19 M. Yu, C. Zhou, J. Liu, J. D. Hankins and J. Zheng, *Journal of the American Chemical Society*, 2011, **133**, 11014–11017.

20 H.-m. Ding and Y.-q. Ma, *Scientific reports*, 2013, **3**, 2804.

21 Y. Hu, T. Litwin, A. R. Nagaraja, B. Kwong, J. Katz, N. Watson and D. J. Irvine, *Nano letters*, 2007, **7**, 3056–3064.

22 P. Loganathan and M. M. Magzoub, *Biophysical Journal*, 2020, **118**, 477a.

23 P. Swietach, R. D. Vaughan-Jones, A. L. Harris and A. Hulikova, *Philosophical Transactions of the Royal Society B: Biological Sciences*, 2014, **369**, 20130099.

24 B. A. Webb, M. Chimenti, M. P. Jacobson and D. L. Barber, *Nature Reviews Cancer*, 2011, **11**, 671–677.

25 J.-H. Lee, J.-t. Jang, J.-s. Choi, S. H. Moon, S.-h. Noh, J.-w. Kim, J.-G. Kim, I.-S. Kim, K. I. Park and J. Cheon, *Nature nanotechnology*, 2011, **6**, 418–422.

26 J. M. Jagtap, A. K. Parchur and G. Sharma, *Intelligent Nanomaterials for Drug Delivery Applications*, Elsevier, 2020, pp. 43–59.

27 A.-R. Lupu, T. Popescu and M. Stojanović, *Environmental Nanotechnology Volume 3*, Springer, 2020, pp. 47–87.

28 G. Canavese, A. Ancona, L. Racca, M. Canta, B. Dumontel, F. Barbaresco, T. Limongi and V. Cauda, *Chemical Engineering Journal*, 2018, **340**, 155–172.

29 O. K. Kosheleva, T.-C. Lai, N. G. Chen, M. Hsiao and C.-H. Chen, *Journal of nanobiotechnology*, 2016, **14**, 46.

30 Z. Ashikbayeva, D. Tosi, D. Balmassov, E. Schena, P. Saccomandi and V. Inglezakis, *Nanomaterials (Basel, Switzerland)*, 2019, **9**, year.

31 R. K. Harishchandra, M. Saleem and H.-J. Galla, *Journal of the Royal Society Interface*, 2010, **7**, S15–S26.

32 D. Kondej and T. R. Sosnowski, *Environmental Science and Pollution Research*, 2016, **23**, 4660–4669.

33 J. J. Schüer, C. Wölk, U. Bakowsky and S. R. Pinnapireddy, *Colloids and Surfaces B: Biointerfaces*, 2020, **188**, 110750.

34 J. J. Schüer, A. Arndt, C. Wölk, S. R. Pinnapireddy and U. Bakowsky, *Langmuir*, 2020.

35 K. Yue, X. Sun, J. Tang, Y. Wei and X. Zhang, *International journal of molecular sciences*, 2019, **20**, 3281.

36 S. I. Hossain, N. S. Gandhi, Z. E. Hughes, Y. Gu and S. C. Saha, *Biochimica et Biophysica Acta (BBA)-Biomembranes*, 2019, **1861**, 1458–1467.

37 A. Verma and F. Stellacci, *small*, 2010, **6**, 12–21.

38 X. C. He, M. Lin, F. Li, B. Y. Sha, F. Xu, Z. G. Qu and L. Wang, *Nanomedicine*, 2015, **10**, 121–141.

39 S. Sharifi, S. Behzadi, S. Laurent, M. L. Forrest, P. Stroeve and M. Mahmoudi, *Chemical Society Reviews*, 2012, **41**, 2323–2343.

40 A. Chakraborty, C. Dalal and N. R. Jana, *Langmuir*, 2018, **34**, 13461–13471.

41 E. Rascol, J.-M. Devoisselle and J. Chopineau, *Nanoscale*, 2016, **8**, 4780–4798.

42 N. Azman, L. Bekale, T. X. Nguyen and J. C. Y. Kah, *Nanoscale*, 2020, **12**, 14021–14036.

43 E. S. Melby, A. C. Mensch, S. E. Lohse, D. Hu, G. Orr, C. J. Murphy, R. J. Hamers and J. A. Pedersen, *Environmental Science: Nano*, 2016, **3**, 45–55.

44 A. C. Mensch, E. S. Melby, E. D. Laudadio, I. U. Foreman-Ortiz, Y. Zhang, A. Dohnalkova, D. Hu, J. A. Pedersen, R. J. Hamers and G. Orr, *Environmental Science: Nano*, 2020, **7**, 149–161.

45 S. Nangia and R. Sureshkumar, *Langmuir*, 2012, **28**, 17666–17671.

46 T. Pfeiffer, A. De Nicola, C. Montis, F. Carla, N. F. van der Vegt, D. Berti and G. Milano, *The journal of physical chemistry letters*, 2018, **10**, 129–137.

47 A. Ridolfi, L. Caselli, C. Montis, G. Mangiapia, D. Berti, M. Brucale and F. Valle, *Journal of Microscopy*, 2020.

48 O. Borozenko, M. Faral, S. Behyan, A. Khan, J. Coulombe, C. DeWolf and A. Badia, *ACS Applied Nano Materials*, 2018, **1**, 5268–5278.

49 S. L. Selladurai, R. Miclette Lamarche, R. Schmidt and C. E. DeWolf, *Langmuir*, 2016, **32**, 10767–10775.

50 L. Wang, P. Quan, S. H. Chen, W. Bu, Y.-F. Li, X. Wu, J. Wu, L. Zhang, Y. Zhao, X. Jiang *et al.*, *ACS nano*, 2019, **13**, 8680–8693.

51 S. S. You, C. T. Heffern, Y. Dai, M. Meron, J. M. Henderson, W. Bu, W. Xie, K. Y. C. Lee and B. Lin, *The Journal of Physical Chemistry B*, 2016, **120**, 9132–9141.

52 M. Paulus, P. Degen, T. Brenner, S. Tiemeyer, B. Struth, M. Tolan and H. Rehage, *Langmuir*, 2010, **26**, 15945–15947.

53 E. M. Curtis, A. H. Bahrami, T. R. Weikl and C. K. Hall, *Nanoscale*, 2015, **7**, 14505–14514.

54 R. Gupta, Y. Badhe, S. Mitragotri and B. Rai, *Nanoscale*, 2020, **12**, 6318–6333.

55 S. Wang, H. Guo, Y. Li and X. Li, *Nanoscale*, 2019, **11**, 4025–4034.

56 S. Tatur, M. Maccarini, R. Barker, A. Nelson and G. Fragneto, *Langmuir*, 2013, **29**, 6606–6614.

57 D. Di Silvio, M. Maccarini, R. Parker, A. Mackie, G. Fragneto and F. B. Bombelli, *Journal of colloid and interface science*, 2017, **504**, 741–750.

58 S. Srivastava, D. Nykypanchuk, M. Fukuto and O. Gang, *ACS nano*, 2014, **8**, 9857–9866.

59 A. C. Mensch, J. T. Buchman, C. L. Haynes, J. A. Pedersen and R. J. Hamers, *Langmuir*, 2018, **34**, 12369–12378.

60 M. Schulz and W. H. Binder, *Macromolecular Rapid Communications*, 2015, **36**, 2031–2041.

61 J. K. Sheavly, J. A. Pedersen and R. C. Van Lehn, *Nanoscale*, 2019, **11**, 2767–2778.

62 R. Chelladurai and J. K. Basu, *Journal of Physics D: Applied Physics*, 2018, **51**, 304002.

63 S. Behyan, O. Borozenko, A. Khan, M. Faral, A. Badia and C. DeWolf, *Environmental Science: Nano*, 2018, **5**, 1218–1230.

64 S. Basiruddin, A. Saha, N. Pradhan and N. R. Jana, *Langmuir*, 2010, **26**, 7475–7481.

65 A. Nelson, *Journal of Applied Crystallography*, 2006, **39**, 273–276.

66 L. G. Parratt, *Physical review*, 1954, **95**, 359.

67 A. Guinier, *X-ray diffraction in crystals, imperfect crystals, and amorphous bodies*, Courier Corporation, 1994.

68 K. Kjaer, *Physica B*, 1994, **198**, 100–109.

69 W. Bu, M. Mihaylov, D. Amoanu, B. Lin, M. Meron, I. Kuzmenko, L. Soderholm and M. L. Schlossman, *The Journal of Physical Chemistry B*, 2014, **118**, 12486–12500.

70 M. K. Ratajczak, E. Y. Chi, S. L. Frey, K. D. Cao, L. M. Luther, K. Y. C. Lee, J. Majewski and K. Kjaer, *Physical review letters*, 2009, **103**, 028103.

71 F. Evers, C. Jeworrek, K. Weise, M. Tolan and R. Winter, *Soft Matter*, 2012, **8**, 2170–2175.

72 E. Y. Chi, C. Ege, A. Winans, J. Majewski, G. Wu, K. Kjaer and K. Y. C. Lee, *Proteins: Structure, Function, and Bioinformatics*, 2008, **72**, 1–24.

73 D. Gidalevitz, Y. Ishitsuka, A. S. Muresan, O. Konovalov, A. J. Waring, R. I. Lehrer and K. Y. C. Lee, *Proceedings of the National Academy of Sciences*, 2003, **100**, 6302–6307.

74 M. Thoma, M. Schwendler, H. Baltes, C. A. Helm, T. Pfohl, H. Riegler and H. Möhwald, *Langmuir*, 1996, **12**, 1722–1728.

75 E. Watkins, C. Miller, D. Mulder, T. Kuhl and J. Majewski, *Physical review letters*, 2009, **102**, 238101.

76 C. Helm, H. Möhwald, K. Kjaer and J. Als-Nielsen, *EPL (Europhysics Letters)*, 1987, **4**, 697.

77 G. Wu, J. Majewski, C. Ege, K. Kjaer, M. J. Weygand and K. Y. C. Lee, *Biophysical journal*, 2005, **89**, 3159–3173.

78 F. Neville, Y. Ishitsuka, C. S. Hodges, O. Konovalov, A. J. Waring, R. Lehrer, K. Y. C. Lee and D. Gidalevitz, *Soft matter*, 2008, **4**, 1665–1674.

79 S. Harguindey, D. Stanciu, J. Devesa, K. Alfarouk, R. A. Cardone, J. D. P. Orozco, P. Devesa, C. Rauch, G. Orive, E. Anitua *et al.*, Seminars in Cancer Biology, 2017, pp. 157–179.

80 D. L. Cheung, *The Journal of chemical physics*, 2014, **141**, 194908.

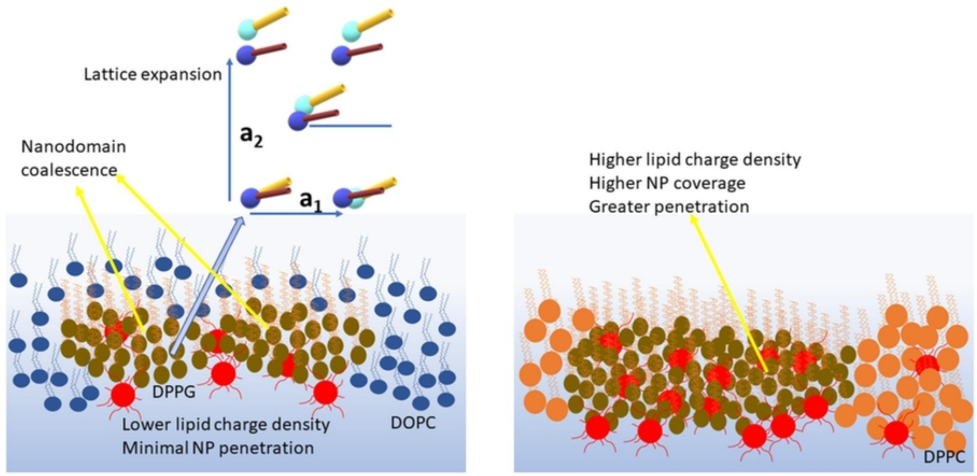


78x39mm (300 x 300 DPI)